# Supporting Information

## Improved Working Model for Interpreting the Excitation Wavelength- and Fluence-Dependent Response in Pulsed Laser-Induced Size Reduction of Aqueous Gold Nanoparticles

**Daniel Werner and Shuichi Hashimoto***

*Department of Ecosystem Engineering, The University of Tokushima, Tokushima 7770-8506, Japan*.

* hashi@eco.tokushima-u.ac.jp

Contents:

**Description of optical properties**

Noble metal NPs absorb and scatter light in the range from UV to near IR.[1-2] The classical interaction of the NPs with light and thus their optical properties are represented by the dielectric function ε. The dielectric function of gold is defined by a sum of an interband term ($\varepsilon_{IB}(\omega)$) that accounts for the response of 5d electrons to a 6sp conduction band and a Drude term ($\varepsilon_D(\omega)$) due to free conduction electrons (Drude model), thus $\varepsilon(\omega) = \varepsilon_{IB}(\omega) + \varepsilon_D(\omega)$.[2] The localized surface plasmon resonance (LSPR) representing the optical properties characteristic of gold NPs originates from the latter term (i.e., photo-excitation of the free electrons). A collective oscillation of photo-excited free electrons on the surface of gold NPs takes place through the interaction with the electromagnetic field of light and exhibits a resonance frequency at 510 to 550 nm of gold nano-spheres depending on the particle radius (extrinsic size effect). By contrast, the interband transition is insensitive to the particle size giving a threshold at 518 nm with a tail at 618 nm. Each term of the dielectric function is divided in a real part ($\varepsilon_1(\omega) = n^2 - k^2$) and an imaginary part ($\varepsilon_2(\omega) = 2nk$), where n is the refractive index and k the absorption coefficient of the metal.

Another important fact is the confinement of free electrons within NPs with diameters smaller than the electron mean free path (40 nm for Au). According to the simplest confinement model, the electrons are additionally damped by a non–elastic scattering process at the inner NP surface, increasing the relaxation frequency or greater damping constant (Γ). Thus the relaxation time of the free electron gas is reduced. The dielectric function (ε(ω)) of a bulk metal has to be modified accordingly (intrinsic size effect), giving rise to a size dependent dielectric function ε(ω, R) shown in eq. 3.

$$\varepsilon(\omega, R) = \varepsilon^{bulk}(\omega) - \varepsilon_D^{bulk}(\omega) + \varepsilon_D(\omega, R) \qquad (3)$$

Here $\varepsilon^{bulk}(\omega)$ describes the dielectric functions of the bulk metal calculated from n and k, experimentally determined by Johnson and Christy[3]. The second and the third terms of eq. 3 are

Drude's dielectric function of the free electron gas of bulk and of the NP with radius R defined by equation 4a and b. It can easily been seen from equation 3 that the optical properties of the free electron gas measured by Johnson and Christy are replaced by the size dependent dielectric function, which considers the intrinsic size effect of NPs, by subtracting the bulk and adding the modified dielectric function,

$$\varepsilon_D^{bulk}(\omega) = 1 - \frac{{\omega_p}^2}{\omega^2 + i\Gamma\omega} \tag{4a}$$

$$\varepsilon_D(\omega, R) = 1 - \frac{{\omega_p}^2}{\omega^2 + i\Gamma(R)\omega} \tag{4b}$$

in which $\omega_p$ [$s^{-1}$] stands for the plasma frequency of the free electron gas defined by $(n_e e^2/\varepsilon_0 m_e^*)^{1/2}$, where $n_e$ is the density of the free electrons [$m^{-3}$], e; the electron charge [As], $\varepsilon_0$; the dielectric constant [$A^2\ s^4\ kg^{-1}\ m^{-3}$] and $m_e^*$; the effective mass of an electron [kg]. The angular frequency ω is defied by a frequency υ multiplied by 2π, Γ describes the relaxation frequency or damping constant, $\Gamma = v_F/\ell$ for the bulk metal, and $\Gamma(R) = v_F(1/\ell + A\ 1/R)$ for metal nano-spheres with diameters smaller than the electron mean free path, where $v_F$ [$m{\cdot}s^{-1}$] is the Fermi velocity, $\ell$ [m] is the electron mean free path, R [m] is the NP radius, and A is a theoretical dependent value (in our case equal to unity). The relaxation frequency Γ is the inverse of the relaxation time τ, which is described as a sum of all possible scattering events within the metal given in eq. 5.

$$\Gamma^{-1} = \tau = \sum_i \tau_i = \tau_{point\_defects} + \tau_{dislocations} + \tau_{grain\_boundaries} + \tau_{e-lattice} + \tau_{e-e} \tag{5}$$

The first three terms on the right hand side of eq. 5 are fixed relaxation times defined by the inner structure of each nanoparticle and the last two terms, the electron – lattice and the electron –

electron scattering (relaxation) time, depend on the temperatures $T_e$ and $T_l$ of the system. The values for gold used in our calculations are given in a textbook by Kittel[4] or one by Ashcroft[5].

The absorption and scattering properties of spherical metal nanoparticles are well described by the Mie theory, where the absorption and scattering probabilities are represented by the absorption cross section $C_{abs}$ [$m^2$], the scattering cross section $C_{sca}$ [$m^2$], and the extinction cross section $C_{ext}$ that is the sum of both ($C_{ext} = C_{sca} + C_{abs}$). In Mie's approach, the absorption and scattering of light originate from the free electron oscillations driven by the oscillating electric and magnetic field of the incident light. Depending on the metal sphere, oscillations from the dipole mode up to higher orders, such like quadrupole or octapole oscillations, are possible. These oscillations were later defined as so called plasmon modes.

Mie solved the Maxwell equations for a dielectric sphere dependent on the particle radius as well as the dielectric function and permittivity of the surrounding medium, where he obtained a set of potentials describing the input, output and inner electromagnetic fields of the sphere. The final formulations for the cross sections, which are commonly used in the literature[2], are described in eq. 6.

$$C_{ext} = \frac{2\pi}{\lambda}\sum_{L=1}^{\infty}(2L+1)\Re\{a_L + b_L\} \tag{6a}$$

$$C_{sca} = \frac{2\pi}{\lambda}\sum_{L=1}^{\infty}(2L+1)\left(|a_L|^2 + |b_L|^2\right) \tag{6b}$$

$$C_{abs} = C_{ext} - C_{sca} \tag{6c}$$

$\lambda$ and L are the wavelength of incident light and the order of oscillation modes, i. e. L = 1 for the dipole and L = 2 for the quadrupole mode. The Mie coefficients $a_L$ and $b_L$ are described in eq. 7.

$$a_L = \frac{m\psi_L(mx)\psi'_L(x) - \psi'_L(mx)\psi_L(x)}{m\psi_L(mx)\eta'_L(x) - \psi'_L(mx)\eta_L(x)} \tag{7a}$$

$$b_L = \frac{\psi_L(mx)\psi'_L(x) - m\psi'_L(mx)\psi_L(x)}{\psi_L(mx)\eta'_L(x) - m\psi'_L(mx)\eta_L(x)} \tag{7b}$$

The functions, $\psi_L$, $\eta_L$, and their derivatives are half–integer Bessel functions of the first and second kind, which have to be solved for each dielectric sphere. The argument $m = \tilde{n}/n_m$ defines the ration of the complex refractive index of the sphere to the refractive index of the surrounding medium and $x = |k|\,R$ is the size parameter as the product of the wave vector and the sphere radius.

**Numerical simulations**

The present differential equations and integral functions are only numerically solvable because of their temperature dependent coefficients, their linking to other equations and the complexness of the EDOS, which is given by numerical data. Therefore, we transformed the coupled-differential heat equations into numerical equations with finite-difference operators. By applying the operators for forward – time $\delta^+$ and central – space $\delta$, given in equation 16d and e, the set of differential equations (see eq. 8) were transformed to:

$$C_e\left(T_e^n\right)\delta_t^+ T_e^n = -g\left(T_e^n\right)\cdot\left[T_e^n - T_l^n\right] + \frac{C_{abs}^{\lambda}\left(n_m, R\right)\cdot P\left(n\Delta t\right)}{V_p\left(T_l^n\right)} \tag{16a}$$

$$C_l\left(T_l^n\right)\delta_t^+ T_l^n = g\left(T_e^n\right)\cdot\left[T_e^n - T_l^n\right] - \frac{3h}{R\left(T_l^n\right)}\left[T_l^n - T_{m(0)}^n\right] \tag{16b}$$

$$C_f\delta_t^+ T_{m(m)}^n = k_f\frac{1}{\left(R + m\Delta r\right)^2}\delta_r\left(\left(R + m\Delta r\right)^2\delta_r T_{m(m)}^n\right) \tag{16c}$$

$$\frac{\partial U}{\partial t} = \delta^+ U_m^n = \frac{1}{\Delta t}\left(U_m^{n+1} - U_m^n\right) \qquad forward - time \tag{16d}$$

$$\frac{\partial U}{\partial r} = \delta U_m^n = \frac{1}{2\Delta r}\left(U_{m+1}^n - U_{m-1}^n\right) \qquad central - space \tag{16e}$$

The index t and r in the operators indicate the time and space. The characters n and m are the number of the time and space steps, and Δt and Δr, which are defined as the total simulation time (t) divided by the time step number (n) and the total simulation distance (r) from the NP divided by the space step number (m).

The initial values were simply set to $T_e^0 = T_l^0 = T_{f(m)}^0 = T_{room}$. The boundary conditions at the NP–water interface and at the distance r from the NP is given by eq. 17.

$$T_{m(0)}^{n+1} = T_{m(0)}^{n} + \Delta t \frac{3h}{R\left(T_l^n\right)\rho_f\left(T_{m(0)}^n\right)C_f}\left[T_l^n - T_{m(0)}^n\right] \quad (17a)$$

$$T_{m(M)}^{n} = T_{room} \quad (17b)$$

Here, the integer value M stands for the total number of space steps, and the origin of the space dimension indicated by zero is located at the NP surface. For the Gaussian intensity profile in time of the laser pulse P(t), we applied a delay time of $-2\tau_p$ from the maximum value of the Gaussian pulse profile to obtain a defined starting intensity of the laser pulse (see Fig. S1). The whole model was converted to the numerical form through a C++ source code.

**References**


1. Bohren, C. F.; Huffman, D. R. *Absorption and Scattering of Light by Small Particles*; Wiley: New York, **1983**.
2. Kreibig, U.; Vollmer, M. *Optical Properties of Metal Clusters*; Springer: Berlin, **1995**.
3. Johnson, P. B.; Christy, R. W. *Phys. Rev. B* **1972**, 6, 12, 4370-4379.
4. Kittel, C. *Introduction to Solid State Physics* 7th Ed.; Wiley: New York, **1996**.
5. Ashcroft, N. W.; Mermin, N. D. *Solid State Physics*; Harcourt Brace: Orland, FL, **1976**.

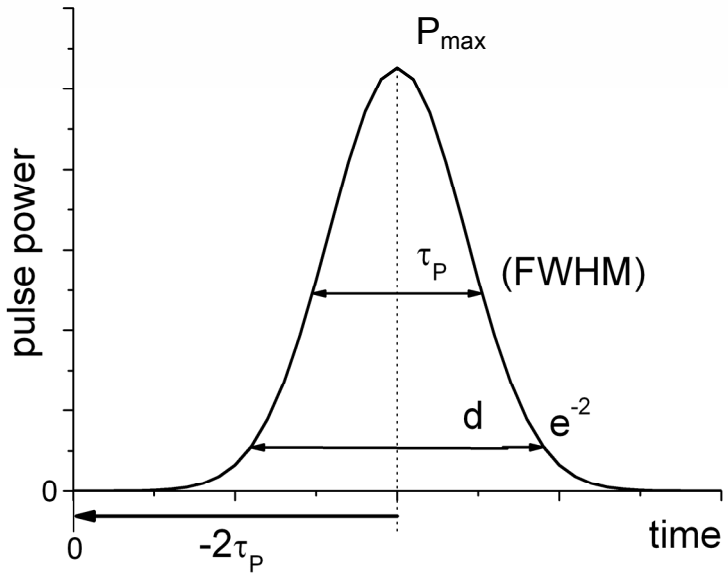


**Fig. S1** Typical Gaussian time profile of pulsed lasers applied to our simulation. Here d denotes the spatial beam diameter, $\tau_P$ the pulse duration and $P_{max}$ the peak power.

**UV-Vis spectrum of 55 nm diameter aqueous gold particles in comparison with the calculated spectrum by Mie theory**

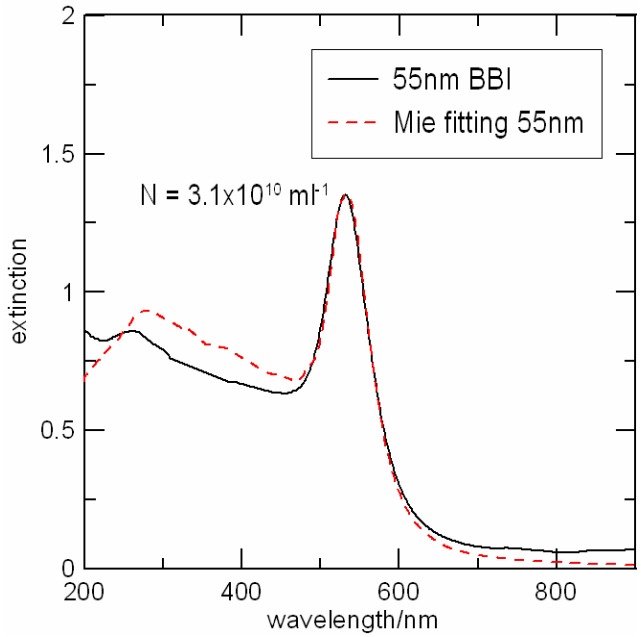


**Fig. S2** Experimental and simulated UV-Vis extinction spectra for aqueous 55 nm diameter gold particles. The solid curve shows the experimental spectrum and the red dotted curve shows that of simulation based on Mie theory including the intrinsic size effect of dielectric functions for 55 nm spherical gold particles in water with a particle concentration of $3.1 \times 10^{10}$ $ml^{-1}$. Concentration given by BBI is $2.6 \times 10^{10}$ $ml^{-1}$, which is in good agreement with the simulation.

**Comparison with the previous experimental results**

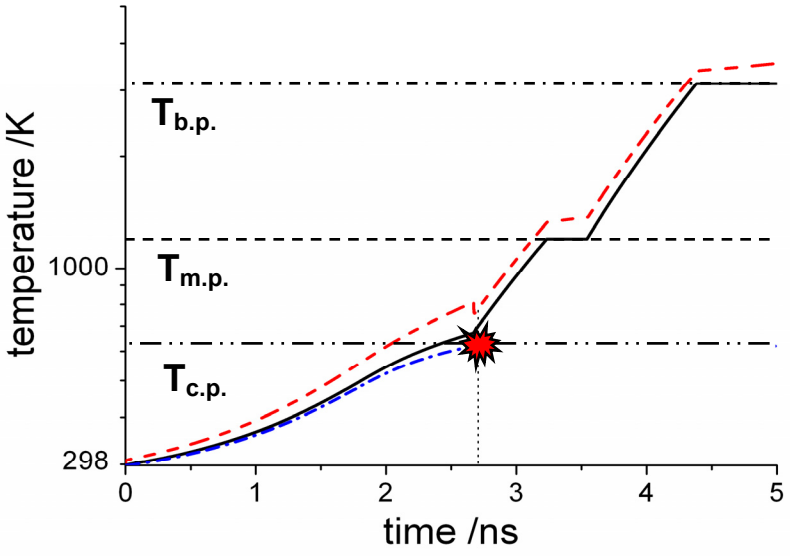


**Fig. S3** Temperature evolution of $T_e$ (red dashed line), $T_l$ (black solid line) and max. $T_m$ (blue dashed-dotted line) calculated for the experimental conditions by Mafune's group (ref. 8): a 355 nm pulse with 10 ns pulse duration at ~283 J $cm^{-2}$ ($P_{max}$ = 26.6 GW $cm^{-2}$). The explosion mark shows the time necessary for the initiation of explosive evaporation of the surrounding water at the NP-water interface. The indices c.p., m.p. and b.p. denote the critical point of water, the melting point and the boiling point of bulk gold.

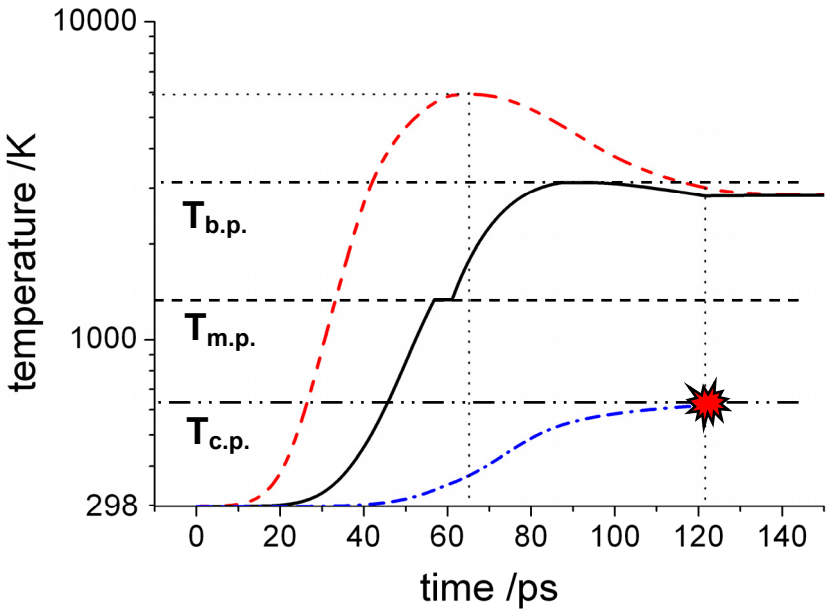


**Fig. S4** Time dependent temperature rise of $T_e$ (red dashed line), $T_l$ (black solid line) and max. $T_m$ (blue dashed-dotted line) according to the experimental conditions by Inasawa's group (ref. 50) for an average fluence of 18 mJ $cm^{-2}$ ($P_{max}$ = 0.59 GW $cm^{-2}$). The horizontal dotted line shows the maximum electron temperature $T_e$ of 6000 K, which is 1300 K below the Rayleigh instability threshold. The explosion mark on the right end shows the time necessary for the initiation of evaporation of the surrounding water at the NP-water interface. The indices c.p., m.p. and b.p. denote the critical point of water, the melting and the boiling point of bulk gold.

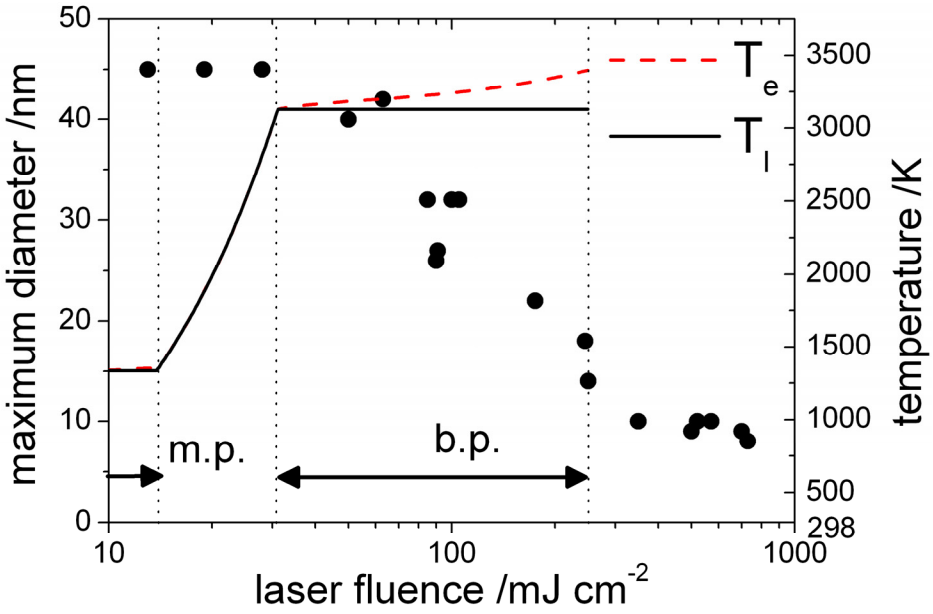


**Fig. S5** Average maximum diameter of gold NPs in aqueous solution vs. laser fluence (black solid circles) according to Koda group's (ref. 11) data (scale on the left side) and temperature curves calculated by us for $T_e$ (red dashed curve) and $T_l$ (black solid curve) under their experimental conditions (scale on the right side). The arrows mark the range of melting and evaporation enthalpies.

**Simulation results for 20 nm gold NPs in aqueous solution irradiated with 266 nm, 5 ns laser pulses**

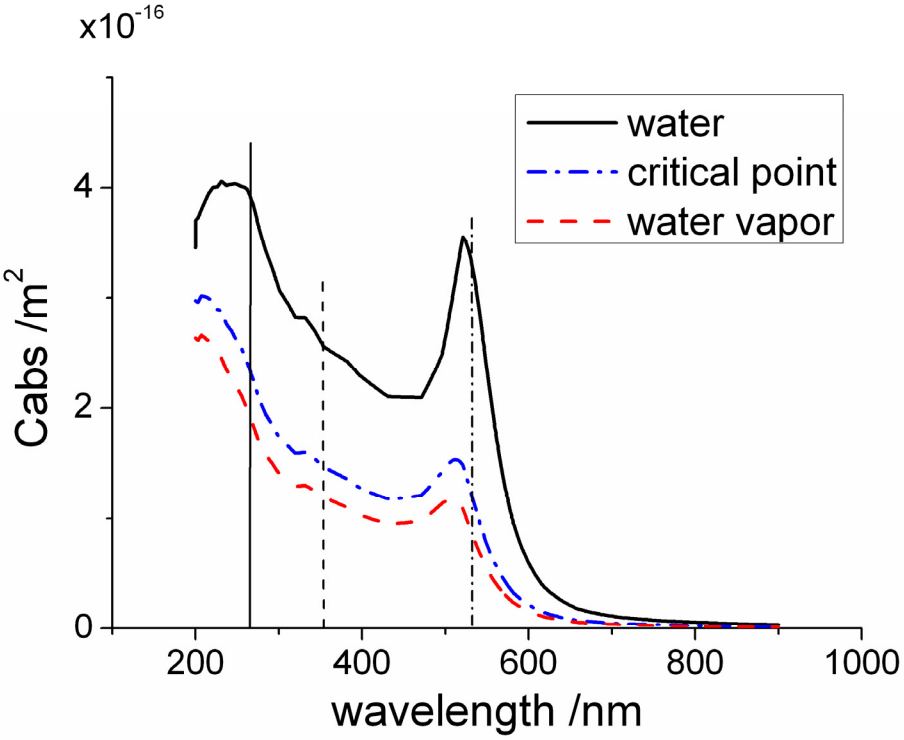


**Fig. S6** Absorption cross section curves as a function of wavelength for a 20 nm diameter gold NP in water of various phases: liquid, vapour, and the critical state. Vertical lines in the figure represent the excitation wavelengths of a nanosecond Nd:YAG laser: the dashed-dotted line, 532 nm; the dashed line, 355 nm; and solid line, 266 nm.

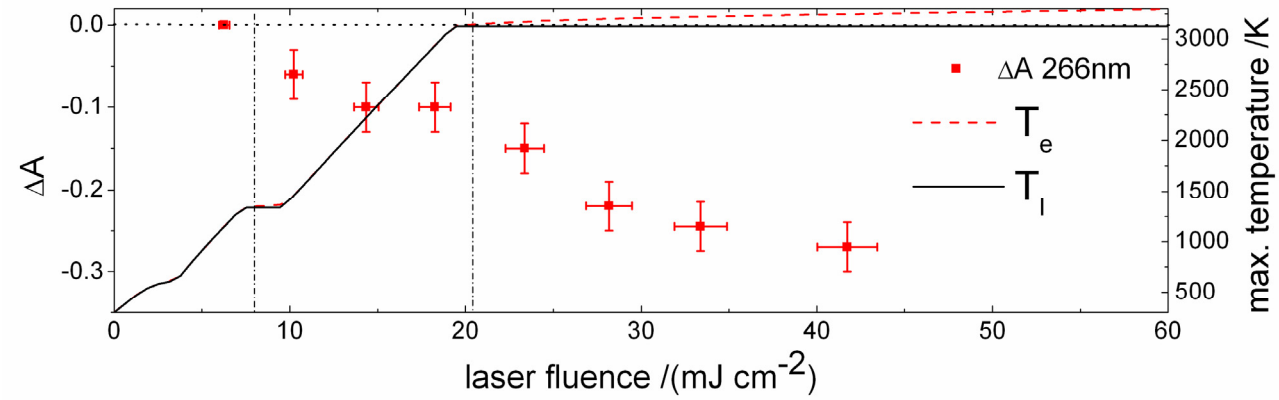


**Fig. S7** Laser fluence dependent temperature evolution of $T_e$ (red dashed line), $T_l$ (black solid line) for a 20 nm aqueous gold NP (scale on the right side) together with the experimental plots of ΔA, the change of SPR band peak intensity after 36000 shots on excitation at 266 nm with various laser fluences (scale on the left side) (ref. 15). The refractive index of the environmental water were assumed to undergo change to n = 1.07 (at the critical point) after explosive bubble formation occurs. The dashed-dotted lines indicate the experimental surface melting and NP fragmentation thresholds. Our simulation is satisfactory enough to estimate the experimental surface melting and evaporation points correctly by taking a greater heat loss compared with that of a 55 nm diameter gold NP into consideration.

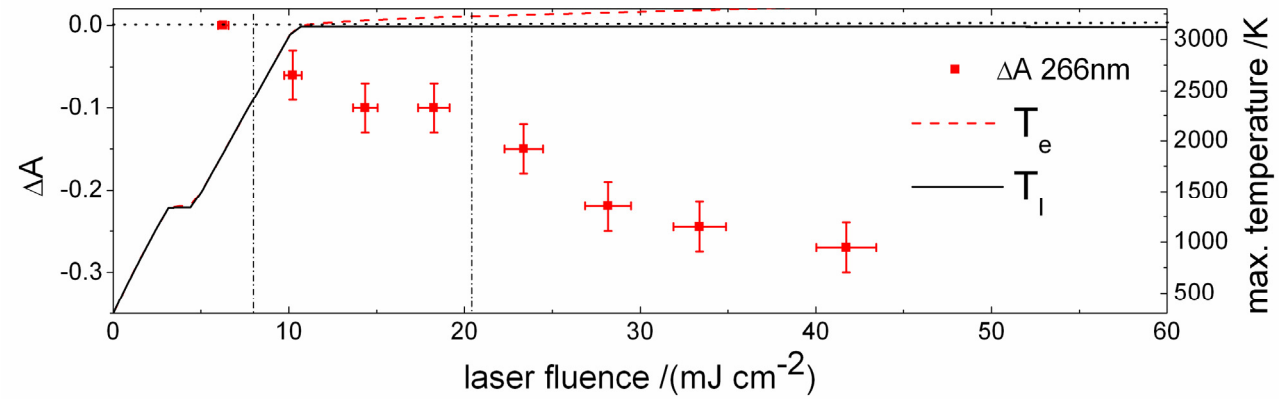


**Fig. S8** Laser fluence dependent temperature evolution of $T_e$ (red dashed line), $T_l$ (black solid line) for a 20 nm aqueous gold NP (scale on the right side) together with the experimental plots of ΔA, the change of SPR band peak intensity after 36000 shots on excitation at 266 nm with various laser fluences (scale on the left side) (ref. 15). Heat losses and the effect of bubble formations on the absorption cross section was neglected here. The dashed-dotted lines indicate the experimental surface melting and NP fragmentation thresholds. Here melting and evaporation temperatures are incorrectly estimated.

**Calculated $T_e$ and $T_l$ corresponding to Fig. 7 in the absence of heat losses**

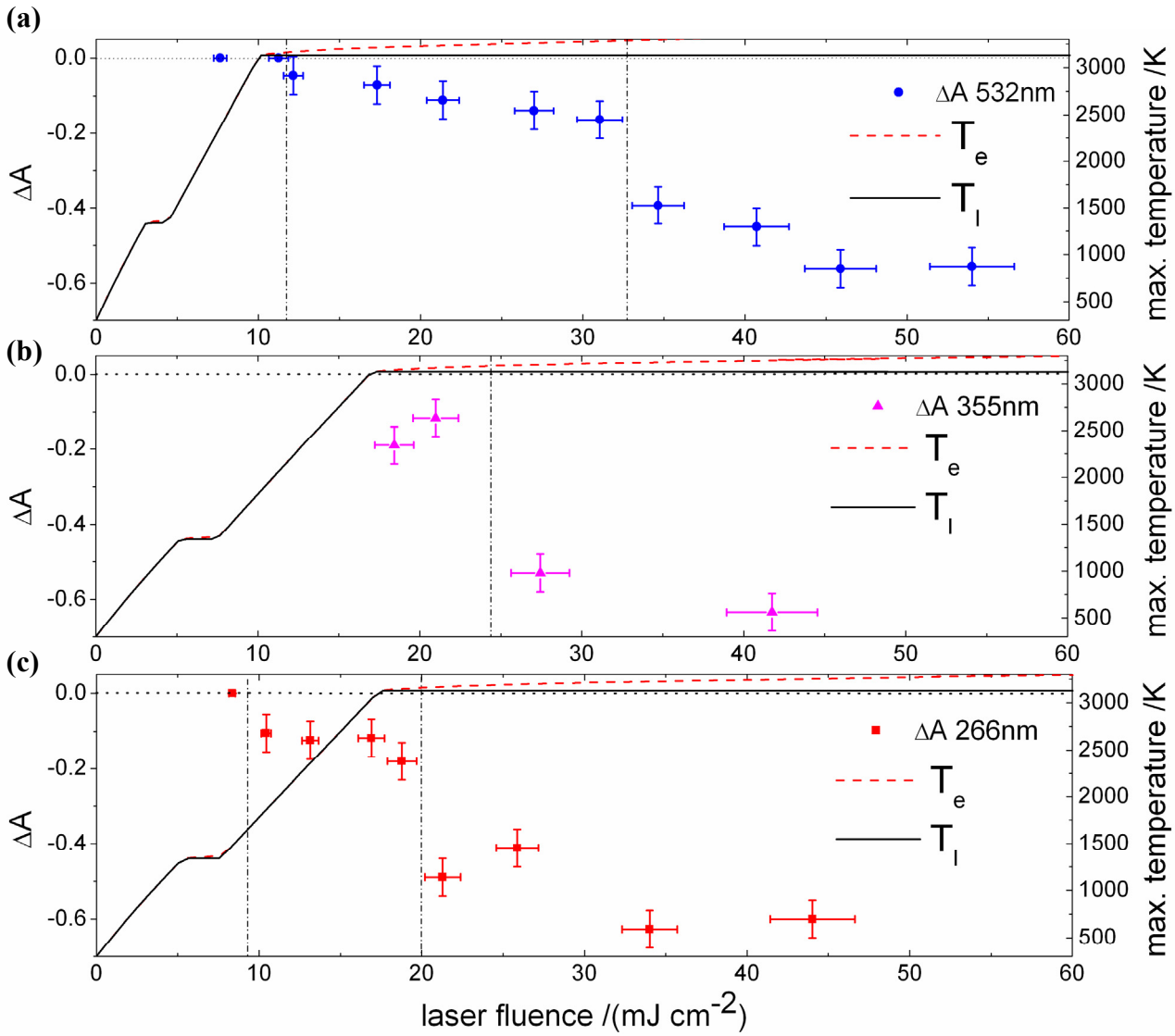


**Fig. S9** Laser fluence dependent temperature evolution of $T_e$ (red dashed line) and $T_l$ (black solid line) for a 55 nm aqueous gold NP (scale on the right side) together with the experimental plots of ΔA, the change of SPR band peak intensity after 36000 shots vs. laser fluence (scale on the left side) on excitation at 532 nm (a), 355 nm (b) and 266 nm (c) (red. 15). Heat losses and the effect of bubble formations on the absorption cross section was neglected here to see the effect of these to the calculated values of $T_e$ and $T_l$. The vertical dashed-dotted lines indicate the experimentally determined surface melting and NP fragmentation thresholds. Different fragmentation efficiency dependent on interband and intraband excitations is observed, which may not be correct.

**TEM images of initial 55 nm gold nanoparticles on laser irradiation of 532 nm pulses at various fluences**

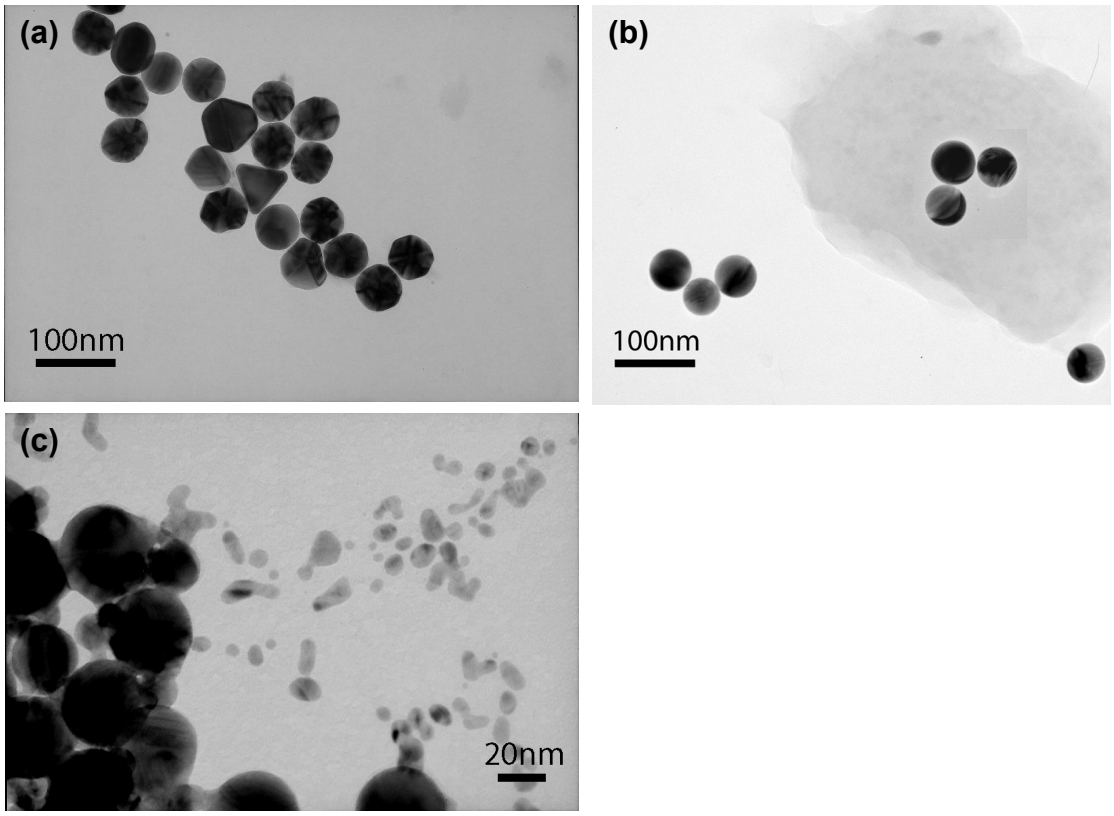


**Fig. S10** TEM images associated with Fig. 7a after 36000 shot irradiation of 532 nm laser at 7.7 mJ $cm^{-2}$ displaying almost intact particles (a), 12.2 mJ $cm^{-2}$ showing the reshaping due to surface melting (b), and 54 mJ $cm^{-2}$. exhibiting the size reduction due to surface evaporation (c). The TEM observations are well correlated with the observed UV-Vis spectral changes.

**Distance-dependent temperature distribution of water in contact with a gold NP at different time delays**

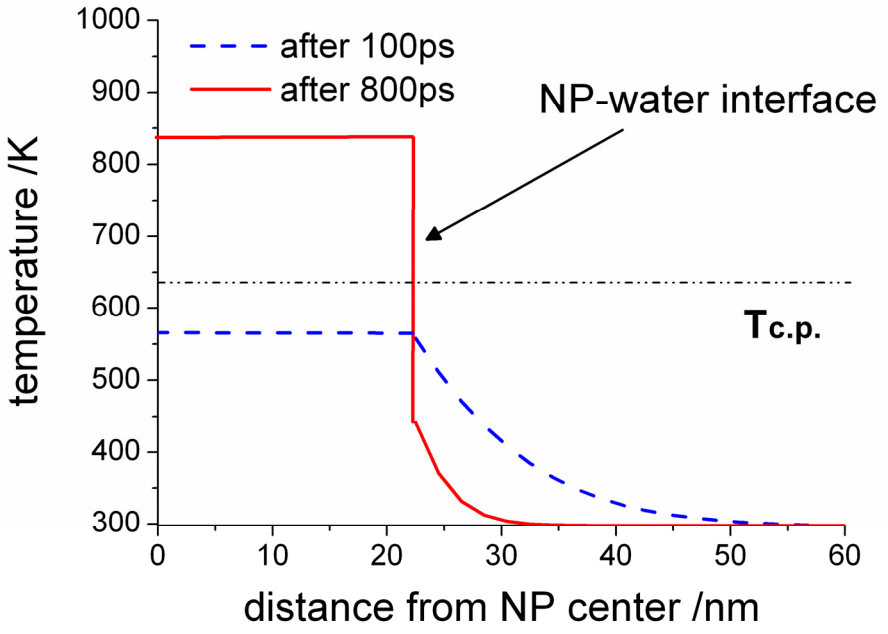


**Fig. S11** Calculated temperature profiles of water surrounding a gold NP of 55 nm diameter excited with a laser fluence of 3.7 mJ $cm^{-2}$ at 400 nm (duration: 300 femtosecond) as function of the radial distance, r from the particle center at time delays of 100 and 800 ps. The temperature inside the particle is assumed to be uniform. At a short delay of 100 ps, a discontinuous drop of the temperature across the NP-water interface is a result of the thermal boundary conductance, h. The temperature calculation was made using eq. 9-c in the text. Temperatue, $T_{c.p.}$ represents the temperature of water at the critical point.

## Table S1: Parameters used for the calculation of $T_e$, $T_l$, and $T_m$

| name | symbol | solid | liquid | vapour |
|---|---|---|---|---|
| specific heat capacity of water | $C_m$ [J kg $K^{-1}$] | | 4182.6 | 2081 |
| density of water | $\rho_m$ [kg $m^{-3}$] | | $1.74831\times10^{6} - 41670.8251\cdot T_m + 505.60719\cdot T_m^{2} - 2.72742\cdot T_m^{3} + + 0.00761\cdot T_m^{4} - 1.08111\times10^{-5}\cdot T_m^{5} + 6.21465\times10^{-9}\cdot T_m^{6}$ | 0.59 |
| heat conductivity of water | $k_m$ [W $m^{-1}$ $K^{-1}$] | | 0.58 | 0.023 |
| lattice heat capacity of gold | $C_l$ [J g $K^{-1}$] | $0.119 + 3.061\times10^{-5}\cdot K^{-1}\cdot T_l$ (6) | 0.149 (6) | |
| density of gold | $\rho_m$ [kg $m^{-3}$] | $m_P/V_P(T_l)$ | $1.74\times10^{4} - 1.44K^{-1}\cdot(T_l - 1337K)$ (7) | |
| thermal expansion coefficient of gold | $\alpha_l$ | $3\cdot(1.24135\times10^{-5} + 5.0786\times10^{-9}K^{-1}\cdot T_l)$ (8) | $1 + 8.3\times10^{-5}\cdot K^{-1}\cdot T_l$ | |
| surface tension of gold | $\sigma$ [N $m^{-1}$] | 8.78 (9) | $1.15 + 0.14\times10^{-3}$ $(T_l - 1337)$ (10) | |
| | | | | |
| melting enthalpy of gold | $H_{melt}$ [J/$m^3$] | $1.212\times10^{9}$ | | |
| lattice constant of fcc unit cell | $a_{fcc}$ [m] | $407.82\times10^{-12}$ | | |
| work function of gold in vacuum | W [eV] | 5.1 | | |
| Fermi energy | $E_F$ [eV] | 5.51 | | |

### References


6. Green, D. W.; Perry, R. H. *Perry's Chemical Engineers' Handbook* 8th Ed.; McGraw-Hill: New York **2007**.
7. Paradis, P. F.; Ishikawa, T.; Koike, N. *Gold Bulletin* **2008**, 41, 242-245.
8. Nix, F. C.; MacNair, D. *Phys. Rev.* **1941**, 60, 597-605.
9. Nanda, K. K; Maisels, A.; Kruis, F. E. *J. Phys. Chem. C* **2008**, 112, 13488-13491.
10. Egry, I.; Lohoefer, G.; Jacobs, G. *Phys. Rev. Lett.* **1995**, 75, 4043-4046.